Parametric Instability of a Vertical Riser under Harmonic Top Motion: Floquet Analysis and Added-Mass Sensitivity

Paulo Victor Sales de Souza

Abstract

A reduced-order stability analysis is presented for the experiment of a submerged vertical flexible cylinder subjected to harmonic top motion. The prescribed axial displacement periodically modulates the tension and hence the transverse geometric stiffness. A Galerkin projection yields independent Mathieu-type modal oscillators with added mass and quadratic drag. Classical Strutt diagrams and Floquet multipliers recover the mode and response frequency associated with the main experimental resonances. The primary 2:1 excitation of the first mode is found to be substantially stronger than the higher-order instabilities. An added-mass sensitivity study then maps uncertainty in the hydrodynamic inertia onto trajectories in the Strutt plane. The principal instability is robust, whereas secondary modal predictions may cross a transition curve for small changes in the added-mass coefficient. The model captures instability onset and dominant frequencies, but its uncoupled modal form does not reproduce the experimental multimodal space-time pattern.

Keywords: parametric excitation; vertical riser; Mathieu equation; Floquet theory; added mass.

1 Introduction

Marine risers are slender structures whose transverse stiffness is strongly affected by axial tension. Vertical motions of a floating unit can therefore excite lateral vibration indirectly: the imposed elongation modulates the tension and produces a time-periodic geometric stiffness. Unlike direct forcing, this mechanism injects energy by varying an internal parameter of the system and can generate subharmonic parametric resonance [1, 2]. Variable-tension risers and tethers have long provided practical examples because their natural frequencies depend directly on geometric stiffness [3, **?**].

Franzini et al. [5] investigated this phenomenon using a vertical flexible cylinder immersed in still water. Figure 1 summarizes the experimental arrangement: the cylinder was clamped at the lower support, submerged over most of its span, and driven by a prescribed vertical motion $h(t)$ at the top. A harmonic top motion with amplitude $A_t/L_0 = 1\%$ was prescribed at frequency ratios $f_t/f_{N,1} = 1/3$, 1, 2, and 3. Modal decomposition, spanwise spectra, and displacement scalograms revealed both Mathieu-like instabilities and responses involving more than one mode. In particular, the 2:1 case displayed dominant first- and second-mode components and an alternating fork-like spatial pattern.

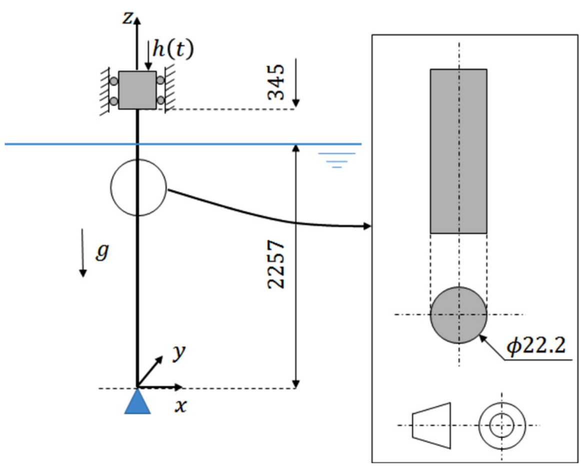

Figure 1: Experimental setup of Ref. [5].

The present study has two objectives. First, a compact Mathieu–Floquet model is used to reproduce the nominal stability classification and dominant frequencies reported in the experiment. Second, the robustness of this classification is quantified with respect to the added-mass coefficient C_A. This extension is motivated by the proximity of several experimental conditions to transition curves and by the known sensitivity of reduced riser models to hydrodynamic coefficients [6].

2 Reduced-order model and stability

For a tension-dominated cylinder, bending stiffness is neglected and the transverse displacement $x(z,t)$ is governed by

$$m_t x_{,tt} + \frac{1}{2}\rho D C_D x_{,t}|x_{,t}| - \frac{\partial}{\partial z}\left(T(z,t)x_{,z}\right) = 0, \qquad (1)$$

where $m_t = m_l + m_{\text{ad}}$ and

$$m_{\text{ad}} = C_A \rho \frac{\pi D^2}{4}. \qquad (2)$$

The tension combines the static contribution of the immersed weight with the modulation caused by the prescribed top motion,

$$T(z,t) = T_t - \gamma(L-z) + \frac{EA}{L_0}A_t\cos(\omega_t t). \qquad (3)$$

Using $x(z,t) = \sin(n\pi z/L)u_n(t)$ and projecting Eq. (1) gives the independent modal equation

$$M_n\ddot{u}_n + \beta_n|\dot{u}_n|\dot{u}_n + [\eta_n + \xi_n\cos(\omega_t t)]u_n = 0, \qquad (4)$$

with

$$M_n = (m_l + m_{\text{ad}})\frac{L}{2},$$
$$\eta_n = \left(\frac{n\pi}{2}\right)^2\left(\frac{2T_t}{L} - \gamma\right), \qquad \xi_n = \left(\frac{n\pi}{2}\right)^2\frac{EA}{L_0}\frac{2A_t}{L}. \qquad (5)$$

Table 1: Nominal experimental parameters used in the model.

Parameter	Value	Parameter	Value
L_0	2.552 m	L	2.602 m
D	0.0222 m	EA	1200 N
m_l	1.19 kg/m	γ	7.88 N/m
T_t	40 N	ρ	1000 kg/m^3
C_A	1.0	C_D	1.2
A_t/L_0	0.01	$f_{N,1}$	0.84 Hz

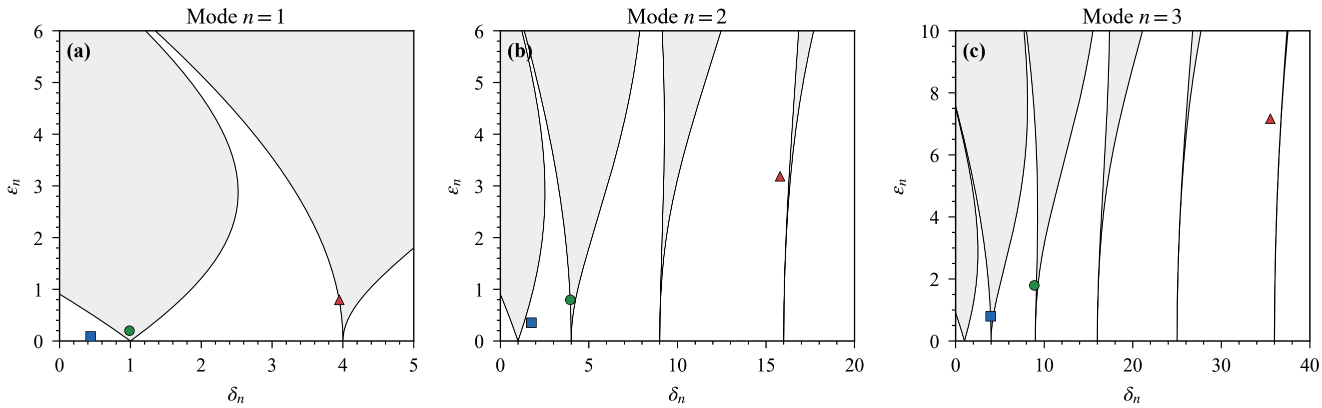

Figure 2: Nominal Strutt diagrams. Red triangles, green circles, and blue squares denote $f_t/f_{N,1}$ = 1, 2, and 3, respectively.

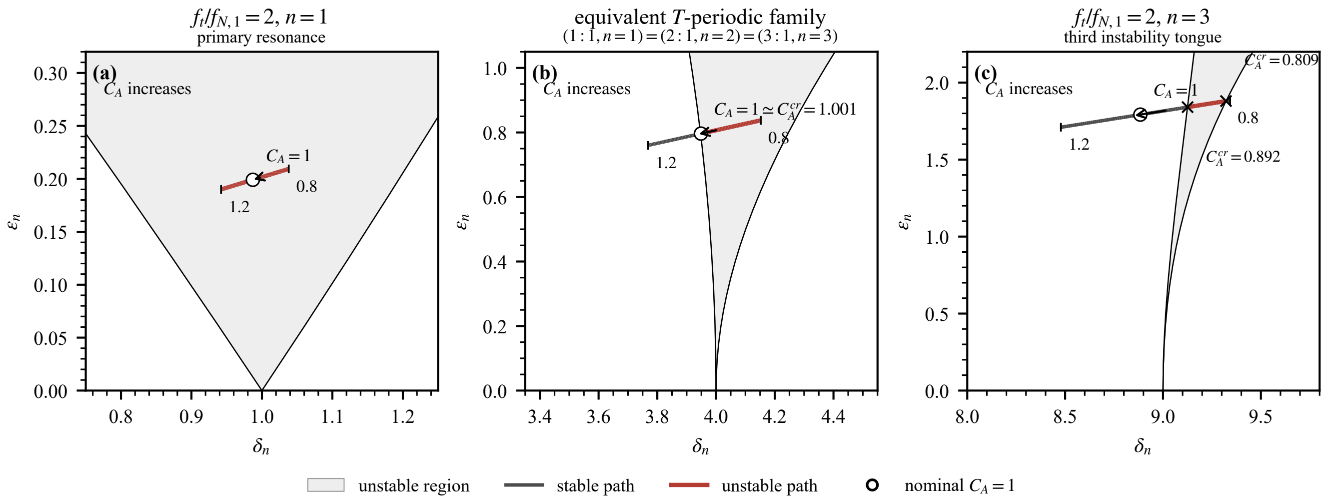

Figure 3: Added-mass trajectories in selected Mathieu tongues. Red and dark gray segments are unstable and stable, respectively; circles indicate the nominal value C_A = 1, and crosses indicate transition values.

The model gives $f_{N,1}$ = 0.835 Hz, compared with the measured 0.84 Hz [5], supporting the string approximation for the low modes.

With $2\tau = \omega_t t$ and after linearization about $u_n = 0$, Eq. (4) becomes

$$u_n'' + [\delta_n + 2\varepsilon_n \cos(2\tau)]u_n = 0,$$

$$\delta_n = \frac{4\eta_n}{M_n\omega_t^2}, \qquad \varepsilon_n = \frac{2\xi_n}{M_n\omega_t^2}. \tag{6}$$

Quadratic drag vanishes in this linearization and affects the finite-amplitude saturation rather than the classical onset boundary [7]. Two fundamental solutions are integrated over one excitation period to form the monodromy matrix. Its eigenvalues ρ_1 and ρ_2 are the Floquet multipliers; $\rho_{\max} = \max|\rho_i| > 1$ indicates instability. The physical growth rate used below is

$$\sigma = f_t \ln \rho_{\max}. \tag{7}$$

A dominant negative multiplier implies a $2T$ response, whereas a positive one implies a T response.

2.1 Numerical implementation

The transition curves were computed from Mathieu characteristic values, with the sign convention in Eq. (6). As an independent check, the two fundamental initial conditions were integrated over $0 \le \tau \le \pi$ and assembled into the monodromy matrix. A fixed grid of 3000 Runge–Kutta steps per period was sufficient to converge $\rho_{\max}$ and the instability boundaries. For the sensitivity analysis, C_A was sampled at 241 points between 0.4 and 1.6, while the physical top frequency and displacement amplitude were kept fixed. Critical values were obtained by interpolating the signed Floquet stability margin between each trajectory and the relevant transition curve. A separate long-time integration of Eq. (4), including quadratic drag, was used only as a post-critical amplitude diagnostic; it does not enter the linear Floquet classification.

2.2 Assumptions and scope

The formulation intentionally isolates the tension-modulation mechanism. The cylinder is treated as a tension-dominated string, so bending stiffness and its end boundary layers are neglected. Still water is assumed; current, vortex-induced vibration, wave loading on the span, and direct lateral forcing are absent. The top motion is monochromatic, and C_A and C_D are constant along the span. Finally, the sinusoidal Galerkin basis produces one scalar equation per mode and therefore suppresses modal coupling by construction.

These assumptions make the model appropriate for testing linear instability onset and periodicity. They are more restrictive for predicting measured amplitudes and traveling-wave patterns. The quadratic-drag term is retained in nonlinear time integration because it provides a physical saturation mechanism, but it disappears from the variational equation at the zero solution. Accordingly, the Strutt and Floquet results below should be read as stability predictions for a controlled baseline, followed by an explicit assessment of what that baseline cannot explain.

3 Results and discussion

3.1 Nominal stability and experimental comparison

Figure 2 shows the classical Mathieu instability tongues and the nominal experimental conditions. The 2:1 first-mode point lies clearly inside the principal instability tongue. In contrast, the $(1{:}1, n = 1)$, $(2{:}1, n = 2)$, and $(3{:}1, n = 3)$ conditions form an equivalent T-periodic family located very close to the transition boundary of the second instability tongue. For the nominal parameters adopted in the present model, the Floquet calculation places these three points marginally on the unstable side of the boundary. Their classification should therefore be regarded as sensitive to small variations in the model parameters.

Table 2 compares the experimental modal results with the nominal Floquet predictions for these selected case–mode pairs. The principal 2:1 first-mode instability has $\sigma = 0.524\ \mathrm{s}^{-1}$ and a negative dominant multiplier; hence, it predicts $f_R = f_t/2 = f_{N,1}$. Its growth rate is approximately 40 times that obtained for the marginal 1:1 first-mode case. The remaining T-periodic predictions have much smaller growth rates and should be interpreted as near-transition results rather than robust instability classifications.

Stable classifications should not be interpreted as a zero experimental response. Direct kinematic effects, initial disturbances, finite-time transients, structural imperfections, and mechanisms omitted from the model can produce bounded spectral components outside a Mathieu tongue. Floquet theory only determines whether an infinitesimal perturbation grows from the trivial state under the adopted linear periodic coefficients.

Table 2: Experimental modal response and nominal Floquet predictions for selected parametrically relevant case–mode pairs.

$f_t/f_{N,1}$	n	u_n^0/D exp.	$f_R/f_{N,1}$ exp.	σ $[\mathrm{s}^{-1}]$	Prediction $f_R/f_{N,1}$
1	1	0.38	1	0.013	1 (T)
2	1	0.63	1	0.524	1 ($2T$)
2	2	0.45	2	0.026	2 (T)
3	3	0.45	3	0.039	3 (T)

Figure 4 summarizes the measured modal amplitudes over all tested frequency ratios. The largest response occurs at 2:1 in the first mode, with $u_1^0/D = 0.63$. The simultaneous value $u_2^0/D = 0.45$ confirms substantial second-mode participation in the same test, consistent with the fork-like pattern reported experimentally. At 3:1, the third-mode amplitude reaches $u_3^0/D = 0.45$, confirming the third-mode-dominated standing wave.

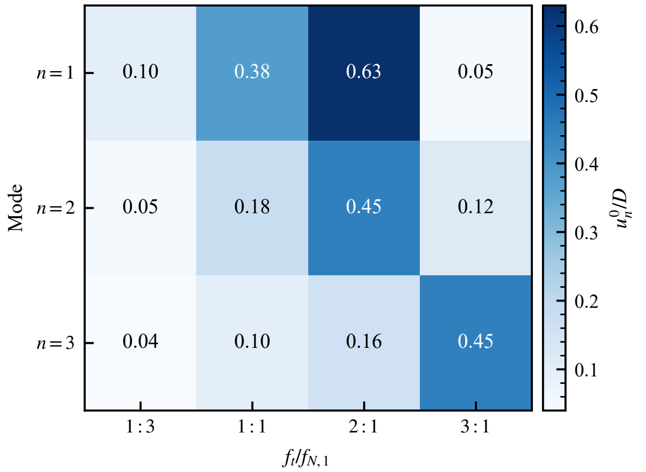

Figure 4: Experimental characteristic modal amplitudes obtained from the modal decomposition reported in Ref. [5].

3.2 Interpretation of the Floquet output

The Strutt classification, multiplier phase, and growth rate answer three different questions. Tongue membership determines whether the trivial state is linearly stable; the sign or phase of the dominant multiplier identifies the periodicity; and σ measures the initial exponential rate. A useful time scale is the amplitude-doubling time

$$t_2 = \frac{\ln 2}{\sigma}. \tag{8}$$

For the 2:1 first-mode case, $t_2 \simeq 1.32$ s, whereas the weak 1:1 first-mode case gives $t_2 \simeq 53.3$ s. Both can therefore appear during the 120 s acquisition, but the latter is much more susceptible to uncertainty and dissipation. Neither value specifies the final amplitude, which results from the balance between parametric energy input and nonlinear damping.

3.3 Added-mass sensitivity

The excitation frequency and top-motion amplitude are now held at their physical experimental values while C_A is varied. From Eqs. (2) and (6), both δ_n and ε_n scale with M_n^{-1}. Increasing C_A therefore moves a case toward the origin along a radial path in the Strutt plane. Indeed,

$$\frac{\varepsilon_n(C_A)}{\delta_n(C_A)} = \frac{\xi_n}{2\eta_n}, \tag{9}$$

which is independent of modal mass. Added mass changes the position along the ray, but not its slope; loss or recovery of stability occurs when that ray intersects a transition boundary.

Figure 3 focuses on $0.8 \le C_A \le 1.2$. The principal 2:1 first-mode path remains unstable throughout this interval, confirming a robust resonance. In contrast, the equivalent family $(1{:}1, n = 1) = (2{:}1, n = 2) = (3{:}1, n = 3)$ crosses the boundary at $C_A^{\mathrm{cr}} = 1.001$. Over the wider calculated range, this family is unstable for approximately $0.680 < C_A < 1.001$. The nominal value is therefore nearly critical. Finally, the 2:1 third-mode case becomes unstable only within the narrow window $0.809 < C_A < 0.892$. This result supports the experimental paper's observation that small changes in hydrodynamic inertia may alter the participation of secondary modes.

The coincident trajectory in Fig. 3(b) follows directly from the string basis. Both η_n and ξ_n scale with n^2, while ω_t^2 scales with n^2 for the sequence $(f_t/f_{N,1}, n) = (1,1), (2,2), (3,3)$. The factors cancel in Eq. (6), so the three cases share the same nondimensional coordinates. This is a prediction of the reduced model, not an assumption that their measured amplitudes must be identical.

Physically, m_{ad} represents the inertia of the surrounding water accelerated with the cylinder; it is not merely a mathematical fitting term. The coefficient C_A compresses this fluid-inertia effect into the reduced model and may depend on geometry, oscillation conditions, and the hydrodynamic idealization. The sensitivity paths therefore quantify how uncertainty in a real fluid force propagates to a stability prediction. They also show why a single nominal value can be adequate for the robust primary tongue but insufficient for secondary modes located near a boundary.

3.4 Relation to the measured responses

The four excitation ratios discussed in detail in Ref. [5] illustrate complementary behaviors. At $f_t/f_{N,1} = 1/3$, the nominal points are stable in the Mathieu model, yet the experiment contains bounded components at the first natural frequency and at the sum and difference frequencies $1 \pm 1/3$. This is not a contradiction: a stable Floquet classification excludes exponential growth from the trivial solution, not forced, transient, or combination-frequency content. At 1:1, the first-mode point lies close to a transition curve and the measured response contains the first two harmonics. The observed traveling waves additionally reflect the spanwise variation of tension, a feature that a fixed sine shape cannot represent.

The 2:1 case provides the clearest parametric result. The strong first-mode $2T$ instability explains the dominant response at $f_{N,1}$, while the weak T instability of the second mode is consistent with a component at $2f_{N,1} = f_t$. The experiment, however, combines these components into an alternating fork-like pattern; independent modal oscillators identify the participating frequencies but does not reproduce the measured modal amplitudes and phases and cannot represent nonlinear modal coupling. Finally, at 3:1, the third-mode T instability predicts a response at $3f_{N,1} = f_t$, in agreement with the narrow-band third-mode standing wave. Thus, agreement is strongest for modal selection and frequency ratios, whereas the spatial wave character is the sharper test of model completeness.

3.5 Model limitations

Agreement is limited to instability onset, mode selection, and dominant frequency. For the experimental 2:1 case, $u_2^0/u_1^0 = 0.45/0.63 \simeq 0.71$ indicates significant participation of both the first and second modes. The independent-mode model, however, predicts a predominantly first-mode response and cannot reproduce the experimental fork-like pattern. This limitation suggests that coupled modes, geometric and hydrodynamic nonlinearities, or more representative mode shapes are required to describe the post-critical response [8], although the present results do not establish a specific energy-transfer mechanism.

The hydrodynamic coefficients play distinct roles: C_A modifies modal inertia, natural frequencies, and stability boundaries, whereas C_D mainly limits the post-critical amplitude through quadratic drag. Therefore, calibrating C_D may improve amplitude estimates but cannot recover the missing modal coupling.

4 Conclusions

A compact Mathieu–Floquet model reproduces the unstable case–mode pairs and dominant response frequencies identified in the vertical-cylinder experiment. The 2:1 first-mode instability is the most robust condition and produces the expected subharmonic $2T$ response. Higher-order instabilities have much smaller growth rates and are sensitive to added mass. In particular, the nominal T-periodic family lies almost exactly at a transition curve, while the possible 2:1 third-mode instability occupies a narrow interval of C_A. The uncoupled model cannot reproduce the measured multimodal spatial pattern; its reliable scope is therefore linear onset and frequency selection. A coupled multimode reduced-order model is the natural next step.

Declaration of Generative AI Use

Generative AI tools were used for language editing, manuscript organization, and assistance with numerical-code development. All formulations, results, interpretations, and conclusions were reviewed and validated by the author.

References

[1] A. H. Nayfeh and D. T. Mook, *Nonlinear Oscillations*. New York: Wiley, 1979.

[2] L. Meirovitch, *Methods of Analytical Dynamics*. Mineola, NY: Dover, 2003.

[3] M. H. Patel and H. I. Park, "Dynamics of tension leg platform tethers at low tension," *Mar. Struct.*, vol. 4, pp. 257–273, 1991.

[4] C. P. Pesce, C. A. Martins, J. A. P. Aranha, M. O. Pinto, R. Ramos Jr., and R. M. da Silva, "Riser technology and industry–university cooperation: Part I—Riser mechanics," in *Proc. Int. Conf. Offshore Mechanics and Arctic Engineering*, vol. 36827, pp. 863–874, 2003.

[5] G. R. Franzini, C. P. Pesce, R. Salles, R. T. Gonçalves, A. L. C. Fujarra, and P. Mendes, "Experimental analysis of a vertical and flexible cylinder in water: Response to top motion excitation and parametric resonance," *J. Vib. Acoust.*, vol. 137, 031010, 2015.

[6] G. R. Franzini, C. C. P. Santos, C. E. N. Mazzilli, and C. P. Pesce, "Parametric excitation of an immersed, vertical and slender beam using reduced-order models: influence of hydrodynamic coefficients," *Mar. Syst. Ocean Technol.*, vol. 11, pp. 10–18, 2016.

[7] D. V. Ramani, W. L. Keith, and R. H. Rand, "Perturbation solution for secondary bifurcation in the quadratically-damped Mathieu equation," *Int. J. Non-Linear Mech.*, vol. 39, pp. 491–502, 2004.

[8] G. R. Franzini and C. E. N. Mazzilli, "Non-linear reduced-order model for parametric excitation analysis of an immersed vertical slender rod," *Int. J. Non-Linear Mech.*, vol. 80, pp. 29–39, 2016.